

Spatiotemporal Optical Vortices From All-Dielectric Bilayer Metagratings

Ken Qin¹, Shijie Kang¹, Aoning Luo¹, Yiyi Yao¹, Xiexuan Zhang¹, Hanchuan Chen¹, Yahan Xiao², Yangsong Ye³, Junqing Shi¹, Xusheng Xia^{4,*}, Haitao Li^{1,*}, and Xiaoxiao Wu^{1,*}

¹*Modern Matter Laboratory and Advanced Materials Thrust, The Hong Kong University of Science and Technology (Guangzhou), Nansha, Guangzhou 511400, Guangdong, China*

²*School of Integrated Circuit Science and Engineering University of Electronic Science and Technology of China, Chengdu 610054, China*

³*Center for Information Photonics and Energy Materials, Shenzhen Institute of Advanced Technology, Chinese Academy of Sciences, Shenzhen 518055, China*

⁴*School of Physics and Mechanics, Wuhan University of Technology, Wuhan 430070, China*

**To whom correspondence should be addressed. E-mails: xsxia@whut.edu.cn (X. Xia), haitaoli@hkust-gz.edu.cn (H. Li) and xiaoxiaowu@hkust-gz.edu.cn (X. Wu)*

Abstract

Spatiotemporal optical vortices (STOVs) carry transverse orbital angular momentum within the space-time domain, rendering them powerful tools for constructing high-dimensional and quantum optical fields. However, most existing approaches rely on highly lossy metallic structures or complex pulse-shaping systems. Here, we propose and experimentally demonstrate an STOV generation scheme based on a bound state in the continuum (BIC) in an all-dielectric bilayer metagrating. By simply introducing a lateral shift between the upper and lower layers of the vertical slots on the dielectric metagrating, the Γ -point BIC transforms into a quasi-BIC (qBIC) with directional radiation and asymmetric coupling. This qBIC further leads to an isolated zero-transmission dip associated with a clear phase singularity and branch cut in the frequency-momentum response, enabling a stable STOV generation under the excitation by a spatiotemporal Gaussian pulse. The multipole analysis of the STOV generation reveals the key role of the asymmetric magnetic dipole of the qBIC. Experimentally, free-space transmission measurements reveal transmission zero and branch cut that agree excellently with theoretical analysis. Therefore, our work provides a scalable new route for manipulating spatiotemporal optical fields on low-loss all-dielectric metasurfaces via only gliding offsets, with potential applications in directional coupling of quantum light sources and spatiotemporal shaping of single-photon wave packets.

Keywords: spatiotemporal optical vortex (STOV); quasi-bound states in the continuum (qBIC); all-dielectric; bilayer metagrating; Kerker effect.

I. INTRODUCTION

Vortices are ubiquitous in wave physics and are characterized by phase singularities accompanied by vanishing field amplitudes at the cores.^{1,2} In optics, such vortex states—referred to as optical vortices (OVs)—carry well-defined orbital angular momentum (OAM)^{3,4} and have enabled a wide range of applications, including optical manipulation,^{5,6} structured light communication,^{7,8} and high-resolution imaging.^{9,10} To date, most studies have focused on longitudinal OAM beams, whose angular-momentum vectors are aligned with the propagation directions.^{11–14} By contrast, transverse OAM beams, in which the OAM is oriented perpendicular to the propagation axis,^{15–17} represent a distinct class of structured light fields.

A typical kind of OVs that carry transverse OAM is spatiotemporal optical vortices (STOVs) that host phase singularities jointly within the space-and-time domain.^{18–20} They hold strong promise for group-delay engineering,^{21,22} quantum wave-packet shaping,^{23,24} and high-dimensional quantum encoding.^{25–27} Yet controllable STOV generation has largely depended on Fourier-optics pulse shapers that imprint helical phases in the frequency-space domain, requiring bulky and complex setups^{28–30} that are difficult to integrate on chip. All-dielectric metasurfaces represent a compact and stable approach,³¹ especially for quantum photonics where low loss is critical: high-index dielectric structures preserve strong scattering and design freedom while suppressing Ohmic loss.³² A kind of all-dielectric spatiotemporal differentiator can generate STOVs within an ultrathin device,³³ but the asymmetric nanostructures are difficult to fabricate with high yield using standard lithography and etching. And surface roughness, etch-induced damage, and nonuniformity introduce additional loss, reducing single-photon count rates and coincidence rates. In particular, symmetry-protected bound states in the continuum (SP-BICs)³⁴ and their symmetry-broken quasi-BIC (qBIC) counterparts support ultrahigh quality factors (Q-factors) and subwavelength field localization.³⁵ However, existing mirror-symmetry-breaking implementations, such as slanted metagratings,³⁶ face a practical scalability barrier for quantum photonics: maintaining a uniform, well-calibrated sidewall tilt and low-scattering interfaces over millimeter- to wafer-scale areas is challenging. Such large-scale fabrication can easily introduce spatially varying symmetry breaking, shift or weaken the targeted singularity conditions, leading to substantial loss and phase noise that compromise STOV mode purity and quantum-state fidelity. In contrast, breaking symmetry via a dislocation between stacked gratings provides a more fabrication-friendly route. Recently, in metallic bilayer-grating platforms, dislocation-based symmetry breaking has been successfully used to couple free-space excitation into unidirectional spoof surface plasmon polariton (SSPP) modes or to produce Fano-type resonant responses.^{37,38} This, in turn, yields a spatiotemporal transfer function featuring a phase singularity with a 2π winding in the frequency-momentum domain, enabling the generation of STOVs. However, it remains unclear how these results can be elevated into a predictive, design-oriented mechanism that establishes a mapping from the

frequency-momentum response to the time-domain STOV waveform, particularly for scalable, low-loss dielectric metagratings where the SSPP-based picture is not directly applicable.

Here, we propose and experimentally demonstrate a qBIC-based scheme for STOV generation through all-dielectric bilayer metagratings as shown in Figure 1(a). A dislocation between stacked gratings breaks the mirror symmetry and converts an SP-BIC into a qBIC with asymmetric radiative coupling. This gives rise to a spiral 2π phase winding around a singularity in the Bloch-wavenumber-frequency ($k_x - f$) parameter space. Under normal-incidence excitation with a spatiotemporal Gaussian pulse, our analysis reveals a clear central null and spiral phase for the transmitted pulse in the periodic direction and time ($x - T$) domain, confirming STOV formation. Furthermore, multipole analysis shows that symmetry breaking induces the orthogonal electric dipole and magnetic dipole,³⁹ whose Kerker-type interference results in the directional and asymmetric radiation.^{40–42} Building on this physical picture, the Lorentz model⁴³ we developed shows that both the transmission zero for various symmetry-breaking parameters and the associated phase branch cut stem from the underlying zero-pole structure in the complex-frequency plane. Experimental measurements in oblique-incidence angle and frequency space ($\theta - f$) further validate the predicted amplitude and phase behavior, showing excellent agreement with theory and simulations. Overall, this work demonstrates qBIC-driven STOV generation on a low-loss dielectric platform largely independent of materials and provides a transferable framework for directional quantum-light coupling, spatiotemporal wave-packet shaping, and high-dimensional photonic encoding.

II. RESULTS

A. BIC in symmetric bilayer metagrating

Figure 1(b) shows a side view of the bilayer metagrating: the metagrating has a period along x direction $a = 3$ mm, a total thickness $h_1 = 1.5$ mm and upper and lower air-slot widths $d = 1$ mm each with depth $h_2 = h_3 = 0.6$ mm. The dielectric material has a refractive index of $n = 3.13$. While keeping the upper air-slot positions fixed, the lower air slots are shifted along the x direction by a distance δd , selectively breaking the mirror symmetry of the structure. The band structure of the metagrating when $\delta d = 0$ mm (symmetry case) as shown in Figure 1(c). The blue solid curve corresponds to the transverse electric (TE) mode, whose electric field is primarily polarized along x direction and which constitutes the resonance branch of interest in this work. The red dashed curve denotes the transverse magnetic (TM) mode, whose electric field is polarized along y direction. Figure 1(d) plots the Q-factor of the TE mode as a function of k_x . The Q-factor diverges at the Γ point, indicating that radiative loss is completely suppressed in the symmetric limit, forming an ideal BIC. Figures 1(e) and 1(f) show the distributions of transmission amplitude and phase of the TE mode, respectively, in the $k_x - f$ space. At the Γ point, the transmission amplitude exhibits a distinct “dark spot” corresponding to an SP-BIC that cannot be excited by an incident

plane wave. And the transmission phase is perfectly symmetric with respect to $k_x = 0$ as is clearly visible in Figure 1(f).

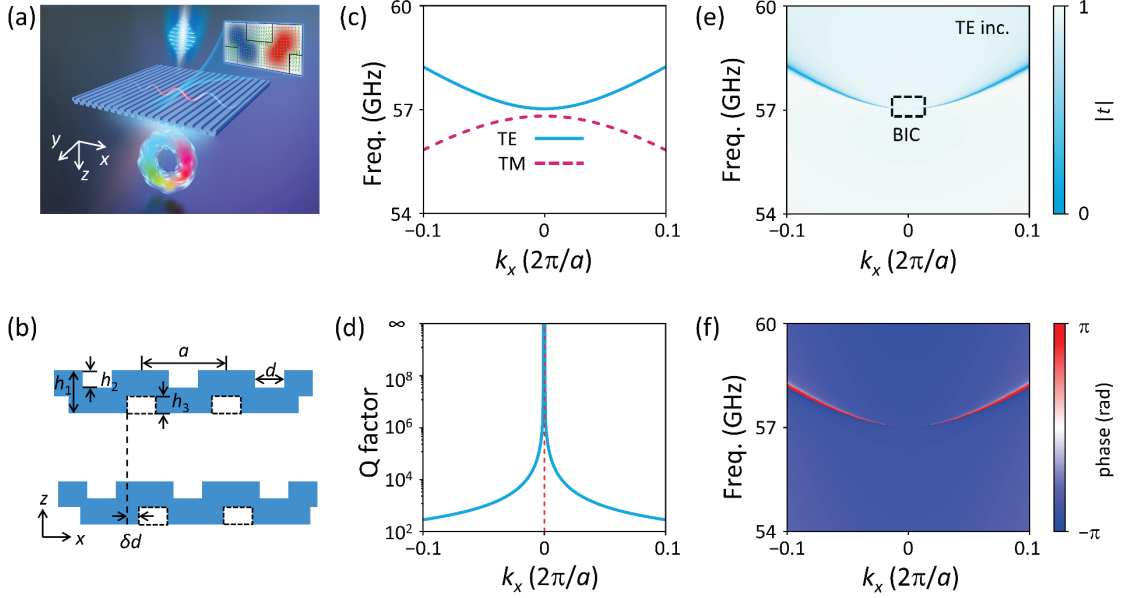


Figure 1. All-dielectric bilayer metagrating and BIC. (a) Schematic illustration of generating an STOV using all-dielectric bilayer metagrating under excitation by a spatiotemporal Gaussian beam. (b) Side view of the bilayer metagrating. Blue regions represent dielectric material with a refractive index $n = 3.13$, and white regions represent air slots. The structure period is a , thickness h_1 , upper and lower air-slot width d , and depth h_2 and h_3 . The upper panel corresponds to the mirror-symmetric case; the lower panel shows the symmetry-broken structure after shifting the lower air slots by δd along the x direction. (c) Band structure under preserved mirror symmetry. The blue solid line denotes the TE mode; the red dashed line denotes the TM mode. (d) Q-factor of the TE mode as a function of k_x with the mirror symmetry. (e) and (f) The amplitude and phase maps of transmission coefficient in the $k_x - f$ space under normal TE incidence.

B. qBIC and STOVs

When a finite slot offset is introduced into the structure, the mirror symmetry of the bilayer metagrating is broken. The SP-BIC degrades into a radiative qBIC. Figure 2(a) shows the normal-incidence transmission spectra for different asymmetry parameters δd . As δd increases, the resonance linewidth gradually broadens and the transmission dip becomes shallower, indicating increased radiative loss and a reduced Q-factor for the qBIC. A quantitative analysis of the radiative quality factor reveals an inverse quadratic dependence on the asymmetry parameter, $Q \propto \delta d^{-2}$, which is a hallmark of SP-BICs perturbed by structural asymmetry³⁵ (see Figure S1 in the Supplementary Materials). Nevertheless, it is worth noting that for all such asymmetry parameters, the transmission dip due to the qBIC remains close to zero, ensuring existence of the zero singularity.

Beyond normal incidence, we plot the transmission amplitude and phase distributions in the $k_x - f$ space. We confirm that a transmission zero emerges at the Γ point (Figure 2(b)), and non-zero transmission arises after deviating from the Γ point.

While the transmission amplitude is symmetric with respect to the $+k_x$ and $-k_x$, we find that a distinct branch cut appears on the $+k_x$ side of the phase map (Figure 2(c)). This branch cut is accompanied by a phase singularity: the phase winds by 2π along a clockwise loop encircling the zero-transmission singular point, indicating a winding number of -1 . Owing to the Fourier correspondence between the $k_x - f$ and $x - T$ domains, such a spectral-domain signature is expected to manifest in the time domain as a central-null amplitude accompanied by a spiral phase structure in the T -domain field.

To verify this correspondence, we perform FDTD simulations for a normally incident pulse with a spatiotemporal Gaussian envelope. The magnetic-field distribution is written as:

$$H_y(x, z, t) = H_0 \exp\left[-\frac{(x-x_0)^2}{w_x^2}\right] \exp\left[-\frac{(T-T_0)^2}{\tau^2}\right] \exp[i(k_0 z - \omega_0 t)] \quad (1)$$

Where w_x is the beam waist radius, x_0 is the spatial center position, τ is the pulse duration, T_0 is the temporal center, ω_0 is the central angular frequency, and k_0 is the wavenumber in the free space, corresponding to propagation along the $+z$ direction.

Figures 2 (d) - (f) show the amplitude and phase evolution of the incident pulse (represented by H_y field) in the $x - T$ space under normal incidence, with $w_x = 45$ mm, $\delta d = 0.1, 0.2, 0.3$ mm, and the corresponding pulse durations $\tau = 10, 6, 3$ ns. To extract the transmitted complex-envelope field in the $x - T$ domain, we apply a Hilbert transform^{44,45} to the simulated time-domain signal to reconstruct the analytic (complex) field. In all three cases, the output exhibits a characteristic vortex-like spatiotemporal interference pattern (upper panel) with a spiral phase (lower panel), consistent with the phase branch-cut behavior in Figure 2(c), and the observed result confirms the winding number of -1 for the generated STOV. The physical origin of the STOV formation can be further elucidated by the instantaneous field distribution in the x - z plane, which reveals a fork-like interference pattern and an associated phase singularity (see Figure S2 in the Supplementary Materials).

As δd is further increased to around 0.4 mm, the associated phase vortices will disappear due to the mode hybridization and thus suppressing STOV generation at large asymmetry (Figure S3 in the Supplementary Materials). Importantly, when the lower air slots shift to the opposite direction ($\delta d < 0$), the transmission zero and phase singularity are preserved, but the phase winding direction is reversed, yielding a STOV with a winding number of $+1$ (see Figure S4 in the Supplementary Materials).

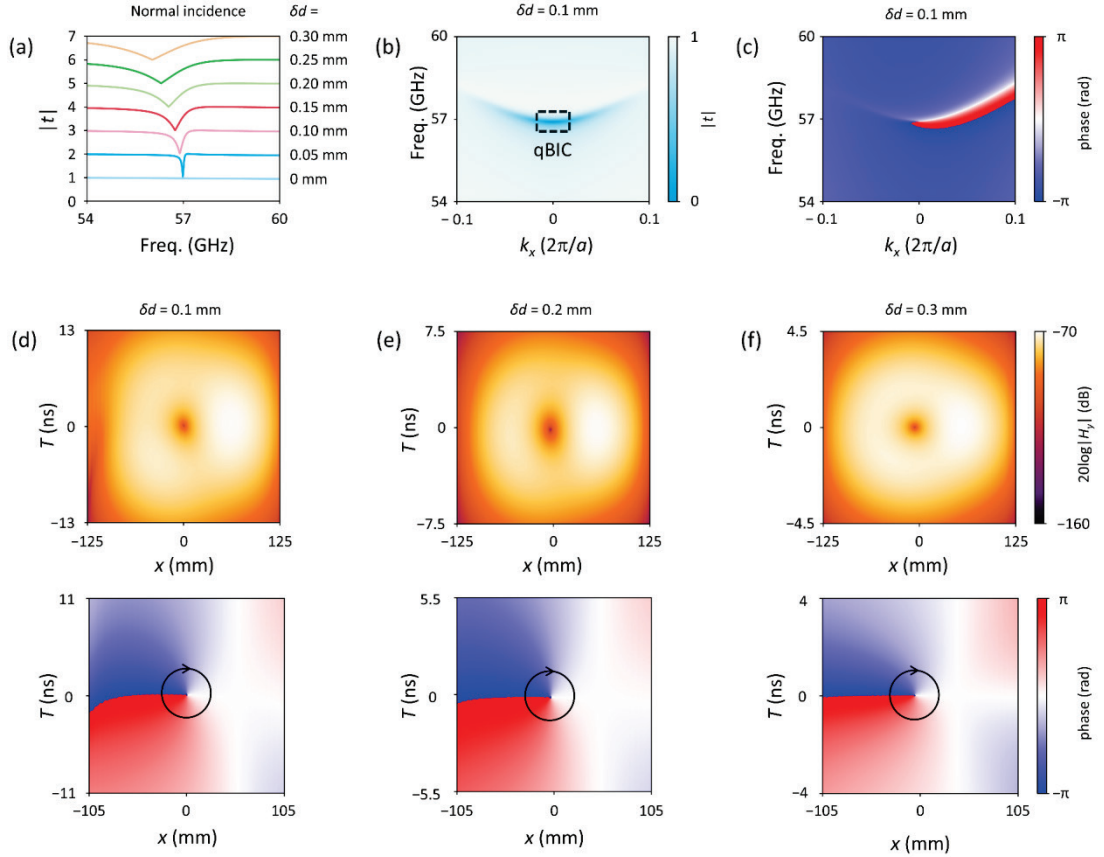


Figure 2. Evolution of STOVs with structural asymmetry. (a) Effect of different values for the asymmetry parameter δd on the transmission spectrum $|t|$ under normal incidence. The spectra are vertically offset by unity in sequence for clarity. (b) and (c) Amplitude and phase distributions of the transmission coefficient in the $k_x - f$ space for $\delta d = 0.1$ mm. (d) - (f) Spatiotemporal evolution of the amplitude and phase of generated STOVs in the $x - T$ space, obtained through simulations of the bilayer metagrating under excitation by a spatiotemporal Gaussian pulse. The beam waist is $w_x = 45$ mm, and the asymmetry parameters are $\delta d = 0.1, 0.2, 0.3$ mm, respectively, with corresponding pulse durations $\tau = 10, 6, 3$ ns.

C. Multipolar interference and directional radiation

To further elucidate the radiation mechanism of the qBIC mode after the structural mirror symmetry is broken, we first perform a multipole decomposition of the radiation fields of the eigenmodes of the structure. Figure 3(a) shows the scattering power of different multipole channels as a function of k_x when $\delta d = 0$ mm. It can be seen that, near $k_x = 0$, the z -component of the electric dipole P_z and the z -component of the toroidal dipole T_z remain dominant and vary only weakly with k_x , whereas the radiation powers of x -component of the electric dipole P_x and y -component of the magnetic dipole M_y are strongly suppressed at the Γ point. When a finite slot shift δd is applied (Figure 3(b)), P_x and M_y increase significantly over the entire k_x axis and exhibit strong k_x -dependence.

Figures 3(c) and 3(d) provide a more intuitive visualization of these multipolar configurations. In the upper schematic, white arrows indicate the magnitude and

direction of H_y at the two ends of a unit cell within one period, and the corresponding T_z and M_y are labeled with black symbols. When $\delta d = 0$ mm, H_y on the two ends have equal magnitude and opposite direction, yielding a spatially antisymmetric magnetic-field distribution within one period. This generates a toroidal dipole current pattern which manifests as a pronounced T_z and an almost vanishing net M_y . After symmetry breaking, although the two ends still carry oppositely directed magnetic fields, their magnitudes become unequal. Consequently, in addition to the original toroidal dipole contribution, a non-zero magnetic dipole M_y emerges. The lower 3D field maps show the H_y distribution in the plane $y = 0$, with red arrows marking the local magnetic-field direction and magnitude, numerically confirming the asymmetric magnetic-field distribution and coexistence of multiple multipoles illustrated in the schematic above.

For different values of k_x , the relative amplitudes and phases of P_x and M_y vary. Their mutual interference, specifically, Kerker-type interference drives a pronounced imbalance between upward and downward radiation. Figure 3(e) shows the H_y field distributions in the upper and lower half-spaces for $\delta d = 0.1$ mm at off- Γ points, with $k_x = -0.05 (2\pi/a)$, 0 and $+0.05 (2\pi/a)$ as the typical examples. When $k_x = -0.05 (2\pi/a)$, the mode radiates more strongly into the lower half-space than into the upper half-space of the metagrating, whereas the situation reverses when $k_x = +0.05 (2\pi/a)$. Specifically, when $k_x = 0$, the radiation fluxes into the upper and lower half-spaces are equal, which is guaranteed by identical air slot depth on the upper and lower layers (see Figure S5 in the Supplementary Materials). Figure 3(f) further quantifies this asymmetric radiation by plotting the ratio between the radiation fluxes into the lower (I_-) and upper half-spaces (I_+) as a function of k_x . With a logarithmic scale of the flux ratio, the monotonic plot reveals that it spans several orders of magnitude and exhibits an exponentially asymmetric behavior depending on k_x . Such strongly directional emission arises from the Kerker-type interference between P_x and M_y , which redistributes radiation preferentially into one half-space. Moreover, the slope of $\log(I_-/I_+)$ is directly controlled by the structural asymmetry parameter δd , indicating that the degree of directional radiation can be continuously tuned via symmetry breaking, as further detailed in Figure S6 of Supplementary Materials.

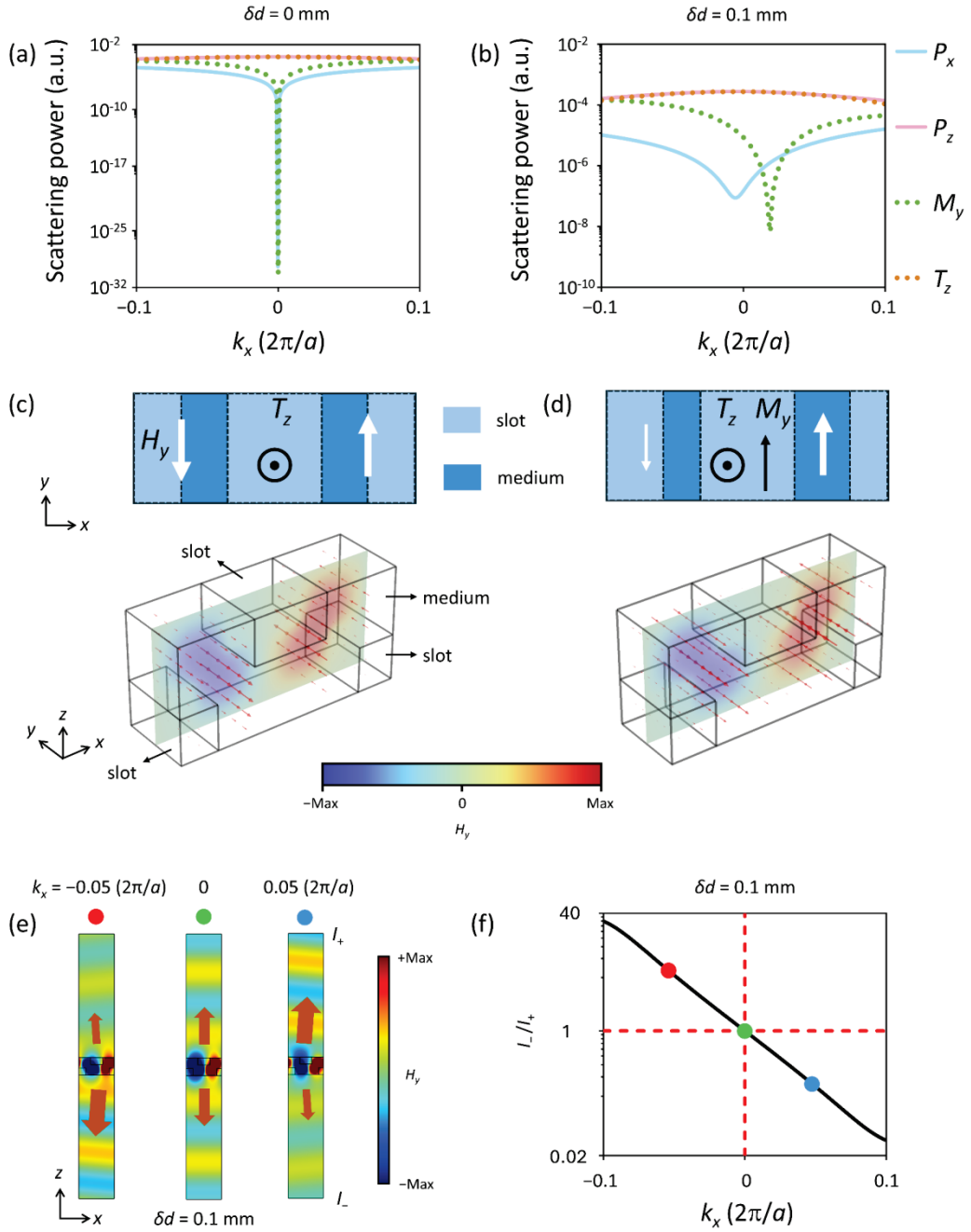


Figure 3. Directional radiation and its multipolar interference origin. (a) - (b) Multipole decomposition of the radiation of the eigenmodes for $\delta d = 0$ mm and $\delta d = 0.1$ mm. The blue solid line, pink solid line, green dashed line, and orange dashed line correspond to P_x , P_z , M_y and T_z , respectively. (c) - (d) Schematics (upper panels) and 3D magnetic-field distributions (lower panels) of the symmetric structure ($\delta d = 0$ mm) and asymmetric structure ($\delta d = 0.1$ mm). In the schematics, white arrows indicate the magnitude and direction of the magnetic field H_y , and black symbols mark the directional configurations of the multipoles T_z and M_y . The lower panels show the distribution of H_y in the $y = 0$ plane, with red arrows indicating the local magnitude and direction of the magnetic field. (e) Distributions of H_y radiated into the upper and lower half-spaces for $\delta d = 0.1$ mm at $k_x = -0.05 (2\pi/a)$, 0 and $+0.05 (2\pi/a)$. The size and direction of the arrows indicate the magnitude and direction of the radiation. (f) For $\delta d = 0.1$ mm, the ratio of the

Poynting-vector flux in the lower half-space (I_-) to that in the upper half-space (I_+) as a function of k_x . Red, green and blue dots represent $k_x = -0.05 (2\pi/a)$, 0 and $+0.05 (2\pi/a)$ that correspond to the dots in Figure 3 (e), respectively.

D. Lorentz oscillator model and phase singularities

Building on the asymmetry of upward and downward radiation about $\pm k_x$, we note that, within the operating frequency band, the structure's emission can be interpreted as the coherent superposition of a narrowband resonant channel dominated by the qBIC mode and a smooth background channel. Accordingly, the transmission coefficient can be analytically approximated using a model with an effective Lorentz oscillator plus background scattering:

$$t(k_x, f) = A(k_x) + \frac{B(k_x) \gamma_0 f_0}{f^2 - f_0^2 - 2if\gamma_0} \quad (2)$$

where $A(k_x)$ is the complex amplitude describing the non-resonant background channel, $B(k_x)$ is the complex coupling coefficient of the effective Lorentz oscillator, and f_0 and γ_0 correspond to the resonance frequency and the radiative linewidth, respectively. Figure 4(a) shows the fitting of this model to the full-wave transmission spectra under illumination from the lower side of the structure at $k_x = \pm 0.05 (2\pi/a)$. The effective Lorentz model accurately reproduces the narrow resonance dip in amplitude and captures the rapid phase variation near resonance, confirming that, for these k_x slices, the transmission is indeed dominated by a single qBIC resonance channel.

To understand the origin of the phase singularities, we analytically continue the transmission coefficient into the complex-frequency ($\text{Re}(f) - \text{Im}(f)$) plane and plot its phase distribution, as shown in Figures 4(b) and 4(c). When $k_x < 0$ (Figure 4(b)), the zero and the pole both lie above the real-frequency axis, and the variation of the frequency of the sinusoidal incidence, that is, sweeping along the real-frequency axis in the complex frequency plane, does not pass across the branch cut, and thus the transmission phase exhibits only a conventional small jump. This corresponds to the absence of a clear branch cut in the $k_x < 0$ region. In contrast, when $k_x > 0$ (Figure 4(c)), the pole remains essentially fixed, but the zero moves across the real-frequency axis into the opposite half-plane. The sweep along the real axis now effectively passes between the zero and the pole, giving rise to an almost 2π topological phase accumulation near the resonance that consists with the prominent phase branch cut observed on the $k_x > 0$ side. In other words, the branch cut that appears only for $k_x > 0$ in Figure 2 originates from a topological rearrangement of the zero-pole pair, triggered by the zero crossing the real-frequency axis.

To further examine the evolution of the zero point with k_x , Figure 4(d) plots the $\text{Im}(f)$ of the zero as a function of k_x for different values of the structural asymmetry δd . As k_x approaches the Γ point, $\text{Im}(f)$ of the zero point converges toward zero, indicating the appearance of a transmission zero near Γ point. Figure 4(e) shows the magnitude of the Lorentz-oscillator coupling strength $|B|$ as a function of k_x . Over the range examined, $|B|$ increases monotonically with k_x : for $k_x < 0$, $|B|$ remains small and the qBIC is only weakly coupled to the radiation channel, corresponding to the zero

not yet having crossed the real-frequency axis, and thus the phase does not exhibit a full 2π winding. When k_x crosses the Γ point into the $k_x > 0$ region, $|B|$ increases significantly; the enhanced coupling “pulls” the zero point to the opposite side of the real-frequency axis, thereby inducing a strong phase branch cut along the real-frequency axis. The phase of B varies slowly versus k_x with no abrupt change near the Γ point as shown in Figure 4(f). This behavior demonstrates that the observed phase singularity and abrupt phase evolution in the transmission response are not caused by a rapid variation of the coupling phase $\arg(B)$ of the Lorentz oscillator, but instead originated from the strong modulation of the coupling magnitude $|B|$ of the oblique incidence with the Lorentz oscillator.

On the other hand, the amplitude and phase of the background term A remain nearly invariant for $k_x \in [-0.05, 0.05]$ ($2\pi/a$) as shown in Figure S7 in Supplementary Materials. This contrast clearly indicates that both the migration of the zero in the complex-frequency plane and the crossing of the branch cut through the real axis of frequency exclusively for $k_x > 0$ originate from the strongly directional coupling with the resonance, rather than from changes in the background scattering. It should be noted that, the zero-pole distribution and its evolution depend on the symmetrical breaking direction. If the lower air slots shifts toward the $-x$ direction instead of the $+x$ direction, the zero-and-pole pair will cross the real axis of frequency in the region $k_x < 0$ correspondingly, and the spiral phase profile will also be reversed, as shown in Figure S8 of the Supplementary Materials.

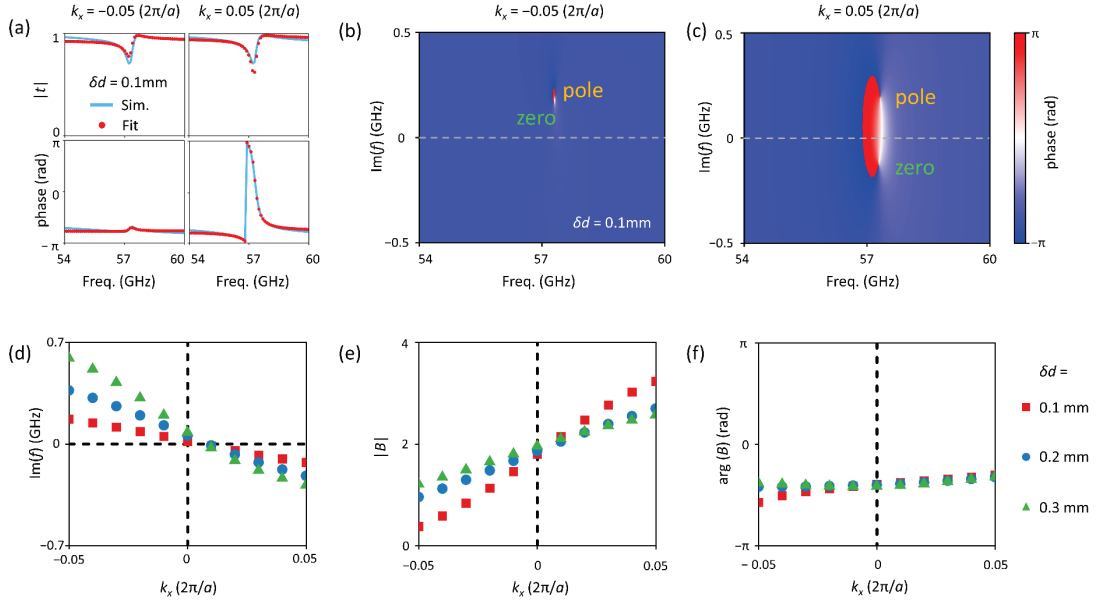


Figure 4. Scattering characteristics and parameter evolution based on the Lorentz oscillator model. (a) Amplitude and phase of the transmission coefficient at $k_x = -0.05 (2\pi/a)$ and $+0.05 (2\pi/a)$ for $\delta d = 0.1$ mm, comparing numerical simulations (blue solid lines) with the Lorentz-model fitting (red dots). (b) - (c) Transmission-phase distributions in the $(\text{Re}(f), \text{Im}(f))$ space for $k_x = -0.05 (2\pi/a)$ and $+0.05 (2\pi/a)$. The locations of the zero and pole are marked. (d) Evolution of $\text{Im}(f)$ of the zero as a function of k_x . (e) - (f) Variation of amplitude and phase of B of the Lorentz-resonant term versus k_x . Red squares, blue circles, and green triangles correspond to

$\delta d = 0.1, 0.2, 0.3$ mm, respectively.

E. Experimental verification and non-Hermitian Effects

To verify the theoretical analyses and numerical simulations presented above, we constructed the millimeter-wave free-space transmission measurement system shown in Figure 5(a) to accurately measure the transmission amplitude and phase of the sample. The experiment employs a millimeter-wave vector-network-analysis system as the test platform, consisting of a vector network analyzer (VNA), a pair of millimeter-wave frequency-extension modules (Freq. Ext. Mod.) operating in the 50 - 75 GHz band, a pair of linear-polarized antennas operating in the corresponding frequency range, and a rotating stage to install the sample and vary the angle of incidence. Figure 5(b) shows the overall and detailed views of the sample in both side and top views. The photograph of the experimental setup is provided in Supplementary Materials Figure S9.

Figures 5(c) and 5(d) show distributions of transmission amplitude and phase in $\theta - f$ space obtained from numerical simulations with a material loss tangent of $\tan\delta = 0.006$. And the reconstructed amplitude and phase of the STOV are shown in the Supplementary Materials Figure S10. Figures 5(e) and 5(f) present the corresponding experimental results. The resonance frequency, angular dispersion trajectory, and the sharp phase jump near the resonance exhibit strong agreement between simulation and experiment. In Figures 5(c) and (e), the regions where the transmission amplitude approaches zero are marked with white dashed loop. As demonstrated in Figure S11 of the Supplementary Materials, for a reasonable range of material loss tangents, the existence of the transmission zero is robust against moderate material loss.

Importantly, in an ideal scenario with no material loss i.e., a fully Hermitian and energy-conserving system, the structural symmetry together with the unitarity of the scattering matrix constrains the position of the transmission zero, forcing it to remain strictly pinned at the Γ point namely $k_x = 0$. However, in real materials, inevitable losses render the effective Hamiltonian and scattering matrix non-Hermitian. From the zero-pole perspective, as the loss tangent increases, $\text{Im}(f)$ of the transmission zero shifts positively along the k_x axis (see Supplementary Materials Figure S12). Consequently, the transmission zero, originally fixed at the Γ point, becomes “detached” from the Γ point and no longer remains at $k_x = 0$.

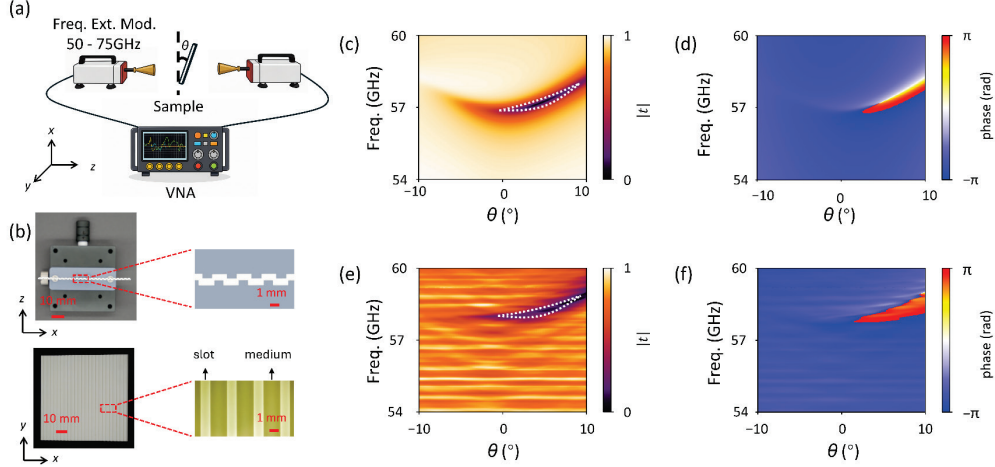


Figure 5. Experimental setup and comparison of simulated and measured transmission characteristics in the $\theta - f$ space. (a) The 50 - 75 GHz frequency-extension modules with horn antennas connected to the VNA to measure the S parameters in the corresponding frequency range. θ is the oblique incidence angle. (b) Side view of the sample and its microstructure (top); top view of the sample and its microstructure (bottom). (c) - (d) Simulated distributions of the transmission amplitude and phase in the $\theta - f$ space, with the material loss tangent set to 0.006. (e) - (f) Corresponding experimentally measured transmission amplitude and phase distributions in the $\theta - f$ space. The regions where the transmission amplitude approaches zero are marked with white dashed loop.

III. CONCLUSION

In this work, we propose and investigate a qBIC-based mechanism for generating spatiotemporal optical vortices (STOVs) in all-dielectric bilayer metagratings. By introducing a tunable lateral shift between the two layers, a symmetry-protected BIC is converted into a radiative qBIC, enabling robust vortex-like and spiral-phase waveforms in the $x - T$ domain under excitation by a spatiotemporal Gaussian pulse. Through multipole analysis, we show that slight symmetry breaking activates the orthogonal electric and magnetic dipoles (P_x and M_y); their Kerker-type interference redistributes the radiated power between the two half-spaces and leads to strongly asymmetric upward and downward radiation. To elucidate the spectral-phase mechanism underlying STOV formation, we further employ an effective Lorentz-oscillator description in which a narrow qBIC resonance coherently interferes with a smooth background channel. This model reproduces the transmission spectra and reveals a clear physical origin of the phase singularity: as the coupling strength $|B|$ increases for oblique momentum, the transmission zero migrates in the complex-frequency plane and is pulled across the real-frequency axis, thereby producing an almost 2π phase winding and the prominent phase branch cut observed in the frequency-momentum response. Finally, free-space measurements in the $\theta - f$ space reproduce the key dispersion and phase signatures, confirming the transmission

zero and the branch-cut behavior. Although experimentally demonstrated at millimeter-wave frequencies, the all-dielectric mechanism is readily scalable to higher frequency regimes and compatible with quantum emitters. Notably, the interlayer lateral shift serves as a simple knob to program a family of tailored wave packets, offering a potentially reconfigurable platform in which both the spatial and temporal waveforms can be tuned, motivating future explorations.

SUPPLEMENTARY MATERIAL

See [Supplementary Material] for the discussion on the radiative Q-factor of the qBIC, magnetic field distributions of the transmitted wave packet, evolution of the transmission response in the k_x - f space, transmission response and time-domain field characteristics for a negative asymmetry parameter, amplitude and phase of background term, experimental free-space S-parameter measurement setup, spatiotemporal response under oblique incidence excitation, and evolution of zero transmission under different material loss tangents.

ACKNOWLEDGMENTS

This research was supported by the National Natural Science Foundation of China (No. 12304348, 62505236), Guangdong Basic and Applied Basic Research Foundation (No. 2025A1515011470), Guangdong University Featured Innovation Program Project (2024KTSCX036), Guangdong Provincial Project (2023QN10X059), Guangzhou-HKUST(GZ) Joint Funding Program (2025A03J3783), Guangzhou Municipal Science and Technology Project (2024A04J4351), and the Fundamental Research Funds for the Central Universities (WUT:104972024RSCbs0023). The authors would like to acknowledge Wave Functional Metamaterial Research Facility (WFMRF) of The Hong Kong University of Science and Technology (Guangzhou) for the experimental support.

AUTHOR DECLARATIONS

The authors have no conflicts to disclose.

REFERENCES

- ¹ J.F. Nye, and M.V. Berry, “Dislocations in wave trains,” *P. Roy. Soc. A-Math. Phys.* **336**(1605), 165–190 (1974).
- ² J. Nye, and F.J. Wright, “*Natural Focusing and Fine Structure of Light: Caustics and Wave Dislocations*,” *Am. J. Phys.* **68**(8), 776–776 (2000).
- ³ G. Molina-Terriza, J.P. Torres, and L. Torner, “Management of the Angular

Momentum of Light: Preparation of Photons in Multidimensional Vector States of Angular Momentum,” *Phys. Rev. Lett.* **88**(1), 013601 (2001).

⁴ A.M. Yao, and M.J. Padgett, “Orbital angular momentum: origins, behavior and applications,” *Adv. Opt. Photon.* **3**(2), 161 (2011).

⁵ Z. Zhang, Y. Shen, S. Yang, J. Luo, Z. Wang, D. Wu, X. Hu, Z. Huang, Y. He, M. Guo, H. Chen, D. Qi, Y. Yao, L. Deng, Z. Sun, and S. Zhang, “Active wavefront shaping for multimode fiber optical tweezers with structured light,” *Opt. and Laser Eng.* **184**, 108639 (2025).

⁶ M.E.J. Friese, T.A. Nieminen, N.R. Heckenberg, and H. Rubinsztein-Dunlop, “Optical alignment and spinning of laser-trapped microscopic particles,” *Nature* **394**(6691), 348–350 (1998).

⁷ F. Ni, Z. Mao, H. Liu, and X. Chen, “Orbital Angular Momentum Communications in Commercial Multimode Fiber with Strong Mode Coupling,” *ACS Photonics* **12**(8), 4423–4431 (2025).

⁸ N. Bozinovic, Y. Yue, Y. Ren, M. Tur, P. Kristensen, H. Huang, A.E. Willner, and S. Ramachandran, “Terabit-Scale Orbital Angular Momentum Mode Division Multiplexing in Fibers,” *Science* **340**(6140), 1545–1548 (2013).

⁹ Y. Zhang, P. Lin, P. Huo, M. Liu, Y. Ren, S. Zhang, Q. Zhou, Y. Wang, Y. Lu, and T. Xu, “Dielectric Metasurface for Synchronously Spiral Phase Contrast and Bright-Field Imaging,” *Nano Lett.* **23**(7), 2991–2997 (2023).

¹⁰ Z. Ye, B. Harrington, and A.D. Pickel, “Optical super-resolution nanothermometry via stimulated emission depletion imaging of upconverting nanoparticles,” *Sci. Adv.* **10**(29), eado6268 (2024).

¹¹ K.A. Forbes, V. Aita, and A.V. Zayats, “Generating optical angular momentum through wavefront curvature,” *APL Photonics* **10**(2), 020801 (2025).

¹² B. Wang, W. Liu, M. Zhao, J. Wang, Y. Zhang, A. Chen, F. Guan, X. Liu, L. Shi, and J. Zi, “Generating optical vortex beams by momentum-space polarization vortices centred at bound states in the continuum,” *Nat. Photonics* **14**(10), 623–628 (2020).

¹³ H. Sroor, Y.-W. Huang, B. Sephton, D. Naidoo, A. Vallés, V. Ginis, C.-W. Qiu, A. Ambrosio, F. Capasso, and A. Forbes, “High-purity orbital angular momentum states from a visible metasurface laser,” *Nat. Photonics* **14**(8), 498–503 (2020).

¹⁴ A.T. O’Neil, I. MacVicar, L. Allen, and M.J. Padgett, “Intrinsic and Extrinsic Nature of the Orbital Angular Momentum of a Light Beam,” *Phys. Rev. Lett.* **88**(5), 053601 (2002).

¹⁵ S.W. Hancock, S. Zahedpour, and H.M. Milchberg, “Mode Structure and Orbital Angular Momentum of Spatiotemporal Optical Vortex Pulses,” *Phys. Rev. Lett.* **127**(19), 193901 (2021).

¹⁶ K.Y. Bliokh, and F. Nori, “Spatiotemporal vortex beams and angular momentum,” *Phys. Rev. A* **86**(3), 033824 (2012).

¹⁷ K.Y. Bliokh, “Spatiotemporal Vortex Pulses: Angular Momenta and Spin-Orbit Interaction,” *Phys. Rev. Lett.* **126**(24), 243601 (2021).

¹⁸ A. Chong, C. Wan, J. Chen, and Q. Zhan, “Generation of spatiotemporal optical vortices with controllable transverse orbital angular momentum,” *Nat. Photonics* **14**(6), 350–354 (2020).

- ¹⁹ C. Wan, J. Chen, A. Chong, and Q. Zhan, “Generation of ultrafast spatiotemporal wave packet embedded with time-varying orbital angular momentum,” *Sci. Bull.* **65**(16), 1334–1336 (2020).
- ²⁰ W. Chen, Y. Liu, and Y.-Q. Lu, “Spatiotemporal Optical Vortices: Toward Tailoring Orbital Angular Momentum of Light in Full Space-Time,” *ACS Photonics* **10**(7), 2011–2019 (2023).
- ²¹ H. Wang, C. Guo, W. Jin, A.Y. Song, and S. Fan, “Engineering arbitrarily oriented spatiotemporal optical vortices using transmission nodal lines,” *Optica* **8**(7), 966 (2021).
- ²² J. Chen, C. Wan, A. Chong, and Q. Zhan, “Subwavelength focusing of a spatio-temporal wave packet with transverse orbital angular momentum,” *Opt. Express* **28**(12), 18472 (2020).
- ²³ Murat Yessenov, L.A. Hall, K.L. Schepler, and A.F. Abouraddy, “Space-time wave packets,” *Adv. Opt. Photon. AOP* **14**(3), 455–570 (2022).
- ²⁴ H.E. Kondakci, and A.F. Abouraddy, “Optical space-time wave packets having arbitrary group velocities in free space,” *Nat. Commun.* **10**(1), 929 (2019).
- ²⁵ F. Feng, G. Hou, Z. Zhang, S. Ma, H. Ma, X. Li, Q. Lin, X. Zhao, M.G. Somekh, and X. Yuan, “Spatiotemporal optical vortex combs,” *Nat. Commun.* **16**(1), 11652 (2025).
- ²⁶ D. Liu, D. Luo, H. Wang, X. Zhang, Z. Tao, D. JiaShaner, Z. Tao, Q. Cao, X. Zhang, G. Fan, and Q. Zhan, “Spatiotemporal Topological Combs for Robust High-Dimensional Information Transmission,” (2025).
- ²⁷ X. Liu, C. Liang, Q. Cao, Y. Cai, and Q. Zhan, “Ultrafast bursts of tailored spatiotemporal vortex pulses,” *Light Sci. Appl.* **14**(1), 361 (2025).
- ²⁸ J. Adams, and A. Chong, “Grating Pair Wavepacket Shaper for Crafting Spatiotemporal Optical Vortices with Arbitrary Tilt Angles,” *Photonics* **12**(2), 126 (2025).
- ²⁹ B.J. Sussman, R. Lausten, and A. Stolow, “Focusing of light following a 4- f pulse shaper: Considerations for quantum control,” *Phys. Rev. A* **77**(4), 043416 (2008).
- ³⁰ S. Huang, P. Wang, X. Shen, and J. Liu, “Properties of the generation and propagation of spatiotemporal optical vortices,” *Opt. Express* **29**(17), 26995 (2021).
- ³¹ S. Jahani, and Z. Jacob, “All-dielectric metamaterials,” *Nature Nanotech.* **11**(1), 23–36 (2016).
- ³² S.M. Kamali, E. Arbabi, A. Arbabi, and A. Faraon, “A review of dielectric optical metasurfaces for wavefront control,” *Nanophotonics* **7**(6), 1041–1068 (2018).
- ³³ J. Huang, J. Zhang, T. Zhu, and Z. Ruan, “Spatiotemporal Differentiators Generating Optical Vortices with Transverse Orbital Angular Momentum and Detecting Sharp Change of Pulse Envelope,” *Laser Photonics Rev.* **16**(5), 2100357 (2022).
- ³⁴ C.W. Hsu, B. Zhen, A.D. Stone, J.D. Joannopoulos, and M. Soljačić, “Bound states in the continuum,” *Nat. Rev. Mater.* **1**(9), 16048 (2016).
- ³⁵ K. Koshelev, S. Lepeshov, M. Liu, A. Bogdanov, and Y. Kivshar, “Asymmetric Metasurfaces with High- Q Resonances Governed by Bound States in the Continuum,” *Phys. Rev. Lett.* **121**(19), 193903 (2018).

- ³⁶ P. Huo, W. Chen, Z. Zhang, Y. Zhang, M. Liu, P. Lin, H. Zhang, Z. Chen, H. Lezec, W. Zhu, A. Agrawal, C. Peng, Y. Lu, and T. Xu, “Observation of spatiotemporal optical vortices enabled by symmetry-breaking slanted nanograting,” *Nat. Commun.* **15**(1), 3055 (2024).
- ³⁷ Y. Zhou, J. Zhan, Z. Xu, Y. Shao, Y. Wang, Y. Dang, S. Zhang, and Y. Ma, “Electromagnetic Spatiotemporal Differentiation Meta-Devices,” *Laser Photonics Rev.* **17**(11), 2300182 (2023).
- ³⁸ Y. Zhou, R. Zou, J. Zhan, Y. Wang, D. Dai, P.K. Choudhury, A. Forbes, and Y. Ma, “Quasi-Bound States in the Continuum on Dislocated Bilayer Metal Gratings for Spatiotemporal Vortex Pulse Generation,” *Laser Photonics Rev.* **19**(9), 2401391 (2025).
- ³⁹ A.B. Evlyukhin, T. Fischer, C. Reinhardt, and B.N. Chichkov, “Optical theorem and multipole scattering of light by arbitrarily shaped nanoparticles,” *Phys. Rev. B* **94**(20), 205434 (2016).
- ⁴⁰ Y.H. Fu, A.I. Kuznetsov, A.E. Miroshnichenko, Y.F. Yu, and B. Luk’yanchuk, “Directional visible light scattering by silicon nanoparticles,” *Nat. Commun.* **4**(1), 1527 (2013).
- ⁴¹ W. Liu, and Y.S. Kivshar, “Generalized Kerker effects in nanophotonics and meta-optics [Invited],” *Opt. Express* **26**(10), 13085 (2018).
- ⁴² A.I. Kuznetsov, A.E. Miroshnichenko, M.L. Brongersma, Y.S. Kivshar, and B. Luk’yanchuk, “Optically resonant dielectric nanostructures,” *Science* **354**(6314), aag2472 (2016).
- ⁴³ R. Colom, E. Mikheeva, K. Achouri, J. Zuniga-Perez, N. Bonod, O.J.F. Martin, S. Burger, and P. Genevet, “Crossing of the Branch Cut: The Topological Origin of a Universal 2π -Phase Retardation in Non-Hermitian Metasurfaces,” *Laser Photonics Rev.* **17**(6), 2200976 (2023).
- ⁴⁴ K.G. Larkin, D.J. Bone, and M.A. Oldfield, “Natural demodulation of two-dimensional fringe patterns I General background of the spiral phase quadrature transform,” *J. Opt. Soc. Am. A* **18**(8), 1862 (2001).
- ⁴⁵ M. Trusiak, M. Cywińska, V. Micó, J.Á. Picazo-Bueno, C. Zuo, P. Zdańkowski, and K. Patorski, “Variational Hilbert Quantitative Phase Imaging,” *Sci. Rep.* **10**(1), 13955 (2020).